



# Stress fluctuations during monotonic loading of dense three-dimensional granular materials

Matthew R. Kuhn<sup>1</sup> · Ali Daouadji<sup>2</sup>

Received: 28 January 2018 / Published online: 4 January 2019  
© Springer-Verlag GmbH Germany, part of Springer Nature 2019

## Abstract

The paper examines the sudden and irregular fluctuations of stress that are commonly observed in DEM and laboratory tests of slow monotonic loading of granular materials. The stress fluctuations occur as stress-drops that are spaced in an irregular, random manner as the material is loaded, and occur at an average rate of about 0.05 drops per particle per one percent of strain. Each fluctuation is accompanied by a drop in the number of contacts and in the number of sliding contacts, a brief increase in the particles' kinetic energy, a reduction in the elastic energy of the contacts, and a reduction in bulk volume. Stress-drops are shown to originate within small regions of the larger assembly and are likely the result of a multi-slip mechanism. An advanced discrete element method (DEM) is used in the study, with non-convex non-spherical particles and an exact implementation of the Hertz-like Cattaneo–Mindlin contact model. The simulations reveal differences with the avalanche phenomenon of amorphous solids, in particular the different scalings of stress-drop magnitude with assembly size and drop frequency.

**Keywords** Granular material · Instability · Micro-mechanics · Energy dissipation · Second-order work · Plasticity · Discrete element method

## 1 Introduction

The past two decades have seen an improved understanding of the deformation and failure of granular materials. This progress has come from advanced testing and imaging methods, from more realistic numerical simulations, and from improved mathematical frameworks for interpreting the results of experiments and simulations. When applied to large-scale engineering problems, the results of these methods have typically been placed in the context of incremental elastoplasticity, which is applied at idealized material points to explain and predict the failure—both diffuse and localized—of bulk specimens. In this approach, failure occurs as

a continuous transition of a material's stiffness that leads to a loss of controllability or to a bifurcation of equilibrium states that are available to support the applied loads. However, experimental studies and numerical simulations show that smaller failures, both micro and meso, occur throughout the approach toward macro-failure. These local “micro-failures” occur when the friction limit is attained at individual contacts or as particles are suddenly rearranged after reaching untenable positions. Micro-failure is most directly expressed during triaxial compression testing as frequent and irregular drops in the deviatoric stress (stress-drops) [1–7], sudden small changes in volume during drained loading [7, 8] or changes in pore pressure during undrained loading, wide fluctuations in the number of inter-particle contacts [9], the emission of acoustic energy from granular materials [7, 10, 11] and from sandstone [12], and sudden increases in the particles' kinetic energy and reductions in internal potential energy [13–15]. The drops in stress and potential energy for frictional granular materials resemble similar events—*avalanches* or *bursts*—that occur in amorphous, glassy solids [16–19], although differences with granular materials are revealed in the current work.

✉ Matthew R. Kuhn  
kuhn@up.edu  
Ali Daouadji  
ali.daouadji@insa-lyon.fr

<sup>1</sup> Donald P. Shiley School of Engineering, University of Portland, 5000 N. Willamette Blvd, Portland, OR 97203, USA

<sup>2</sup> University of Lyon, INSA-Lyon, GEOMAS, 69621 Lyon, France

The confined and localized failures in jammed granular materials occur while the material is strain hardening and prior to the peak strength and diffuse failure, which are reached when the otherwise small, infrequent, and confined failures are sufficiently numerous and organized to produce diffuse macro-failure [20]. This view of deformation challenges an underlying tenet of continuum elastoplasticity: that progress toward failure is a smooth transition of the material state (for example, the continuous alterations of a yield surface and hardening modulus). The paper examines the non-smooth transition of stress and fabric in a 3D granular material during monotonic loading, using numerical discrete element (DEM) simulations to quantify the frequency, intensity, and longevity of the frequent drops and recoveries of stress and to determine the micro-scale mechanisms that are likely responsible.

## 2 Monotonic triaxial compression and non-smooth behavior

We used a series of slow, quasi-static DEM simulations to study the evolution of stress in a granular assembly. The assembly was a cubical box filled with 10,648 smooth non-convex sphere-cluster particles contained within periodic boundaries, with each sphere-cluster composed of seven overlapping, bonded spheres (Fig. 9 in “Appendix” section). Hereafter, we refer to a sphere-cluster of seven overlapping spheres as a single particle. Each such non-convex particle can touch another particle at multiple contacts, thus instilling rotational restraint in a natural way, without resort to rotational contact springs. The particles’ shape, sizes, and arrangement were calibrated to simulate the behavior of the fine-grain poorly-graded medium-dense Nevada Sand (model details are described in “Appendix” section). The particle size range was 0.074–0.28 mm, with  $D_{50} = 0.165$  mm. The assembly was large enough to capture the average material behavior but sufficiently small to prevent meso-scale localization, such as shear bands.

The particles interacted at contacts that were modeled with Hertz-type elastic springs for the normal component of force and with an exact implementation of the frictional Cattaneo–Mindlin interaction for the tangential force component (see [21, 22] and “Appendix” section). A Cattaneo–Mindlin model yields a more faithful representation of the small-strain stiffness of sands, in which stiffness is typically found to be proportional to the mean stress raised to the power of 0.4–0.6. We also conducted simulations with standard linear–frictional contacts, and, aside from the relationship between stiffness and mean stress, the results were qualitatively similar in all respects to those report with Cattaneo–Mindlin contacts. Both Cattaneo–Mindlin and linear–frictional models are rate-independent, such

that the friction coefficient is independent of the loading rate and the rate history. As such, these models do not exhibit the rate-strengthening or rate-weakening that can produce stick-slip or ratcheting behaviors. The initial particle arrangement was isotropic with a confining mean stress  $p = -\frac{1}{3}(\sigma_{11} + \sigma_{22} + \sigma_{33}) = 100$  kPa. The initial dense (jammed) packing had a solid fraction 0.637.

The simulations are of triaxial loading, with a compressive reduction in the  $x_1$  height while maintaining a constant mean stress, by adjusting the  $x_2$  and  $x_3$  widths (i.e., constant- $p$  triaxial loading). With these conditions, any stress fluctuations or local micro-scale mechanisms would be due to deviatoric loading alone. Figure 1 shows the results of a simulation of isobaric (drained), constant- $p$  triaxial compression, in which the  $x_1$  width of the assembly was reduced at constant rate  $\dot{\epsilon}_{11}$  while adjusting the lateral widths to maintain the constant mean stress of 100 kPa. This simulation of constant- $p$  monotonic triaxial compression is the focus of the paper. Figure 1a shows both stress and volume change for the DEM simulation and for a Nevada Sand specimen tested in the VELACS program (the latter being specimen 69–75 at 60% relative density [23]).

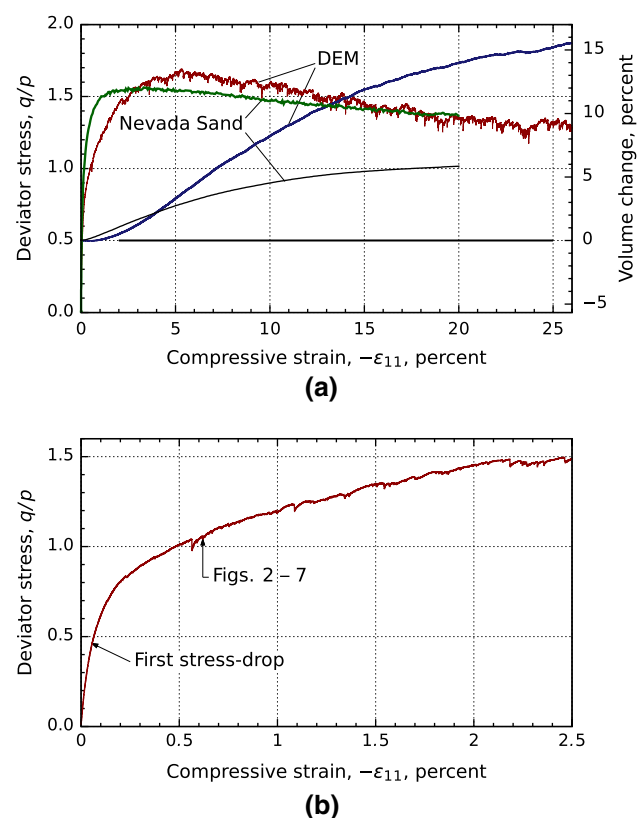


**Fig. 1** a Stress and volume change of Nevada Sand and of DEM simulation for triaxial compression at constant mean stress of 10,648 non-convex sphere-cluster particles (in DEM simulation,  $p_0 = 100$  kPa): the upper lines are stress; whereas, the lower lines are volume change. b Detail of stress for the DEM simulation

## 2.1 Non-smooth transitions in the form of stress-drops

In Fig. 1, we show the deviator stress, the difference  $-q = -(\sigma_{11} - \sigma_{33})$  between the loading and lateral directions, that is developed during drained triaxial compression under constant mean stress (stress is normalized by dividing by the pressure  $p$ , equal to the negative mean stress). The figure exhibits frequent irregular and abrupt changes, which gives the stress-strain plots a rough, raspy, and non-smooth appearance. This characteristic is widely reported, both in simulations [1–3, 5, 24] and in physical experiments [2, 7, 11, 25, 26]. Roux and Combe [27] recognized the propensity for these abrupt changes as an innate attribute of granular materials, and they distinguished two regimes of granular behavior: a small-strain *strictly quasi-static regime* and a *rearrangement regime* at larger strains. In the strictly quasi-static regime at small strains, behavior is relatively smooth, bulk deformation is largely produced by deformations at the contacts, and a progressive reduction in stiffness results from the elimination of contacts in directions of bulk extension. In the second, non-smooth rearrangement regime at larger strain, frictional slip becomes more frequent, bulk deformation is primarily attributed to rearrangements of the contact network, and deformation proceeds with frequent and seemingly abrupt alterations of stress, which we call *stress-drops*, that are caused by the rearrangements. Because these repetitive and abrupt stress-drops are a dominant feature of granular behavior, we sought a better understanding of their origin and effects. Similar stress-drops have also been observed in experiments and in atomistic simulations of amorphous solids that employ Lennard-Jones and other potentials for the atomic interactions [16, 19, 28].

In our simulations, the transition between the smooth and non-smooth regimes occurred at a strain of less than 0.1%, suggesting that the strictly static regime is restricted to strains near the start of loading. The frequency and severity of stress-drops increases with increasing strain, although

these aspects remain steady beyond a strain of 1%. Table 1 summarizes various measures of frequency and severity for the strain ranges of 0–1% and 1–16%, and these results are discussed below. The table is supplemented by Fig. 2, which details the stress and other characteristics during a small period of the non-smooth rearrangement regime, for the range of strains  $-\varepsilon_{11}$  of 0.61–0.66%. More than a dozen stress-drop episodes occurred within this small interval, and dotted lines in the figure delineate three such stress-drops that will be analyzed more closely below. The detail of deviator stress in Fig. 2a closely resembles the experimental results of Michlmayr et al. [11] and of Cui et al. [7] for direct shear and triaxial compression tests on glass beads. Besides deviatoric stress, Fig. 2 details the number of contacts among the particles; the relative number of fully sliding contacts; the number of contacts among the touching particles; the average kinetic energy of the particles; the elastic (Helmholtz free) energy of the assembly; and the volumetric strain. The numbers of contacts and sliding contacts are expressed in non-dimensional form by dividing by the total number of particles, noting that a pair of non-convex sphere-cluster particles can have multiple contacts.

The stress-drops were brief events and had an average (strain) duration of about  $2.5 \times 10^{-6}$  (Table 1 and Fig. 2a). For the small strain increments used in our simulations (increments  $d\varepsilon_{11}$  of  $2 \times 10^{-9}$ ), an average stress-drop spanned more than 1200 DEM strain steps. Although brief, this duration indicates that a stress-drop is not a strictly abrupt event but has a finite duration during which a significant rearrangement of the particles occurs. These rearrangements are likely triggered by a local loss of stability within groups of particles, described later, exhibiting negative second-order work at individual contacts [13, 29]. After a stress-drop is triggered, the stress continues to drop until a new, more stable particle arrangement is reached. The stress-drop is then followed by a period of stress-recovery in which the deviatoric stress increases more gradually than it had decreased during the preceding stress-drop. During

**Table 1** Characteristics of stress-drops during triaxial loading for simulations of 10,648 sphere-cluster particles with mean stress  $p = 100$  kPa

Characteristic	Strain range	
	0–1%	1–16%
Strain $\varepsilon_{11}$ at the first stress-drop	0.00056	–
Number of stress-drops within the strain range	320	7880
Number of stress-drops per particle per 1% strain <sup>a</sup>	0.030	0.049
Mean strain duration of a stress-drop	$2.3 \times 10^{-6}$	$2.7 \times 10^{-6}$
Range of strain durations of stress-drops <sup>b</sup>	$(0.4 - 4.4) \times 10^{-6}$	$(0.4 - 6.0) \times 10^{-6}$
Mean drop in deviator stress, $\langle \Delta q \rangle$	100 Pa	170 Pa
Fraction of total strain engaged in stress-drops	7%	14%
Sum of deviator stress reductions per 1% strain	33 kPa	91 kPa

<sup>a</sup>Number of drops in range divided by 10,648 particles and by 1 or 15 percent range

<sup>b</sup>Values of 10th and 90th percentiles

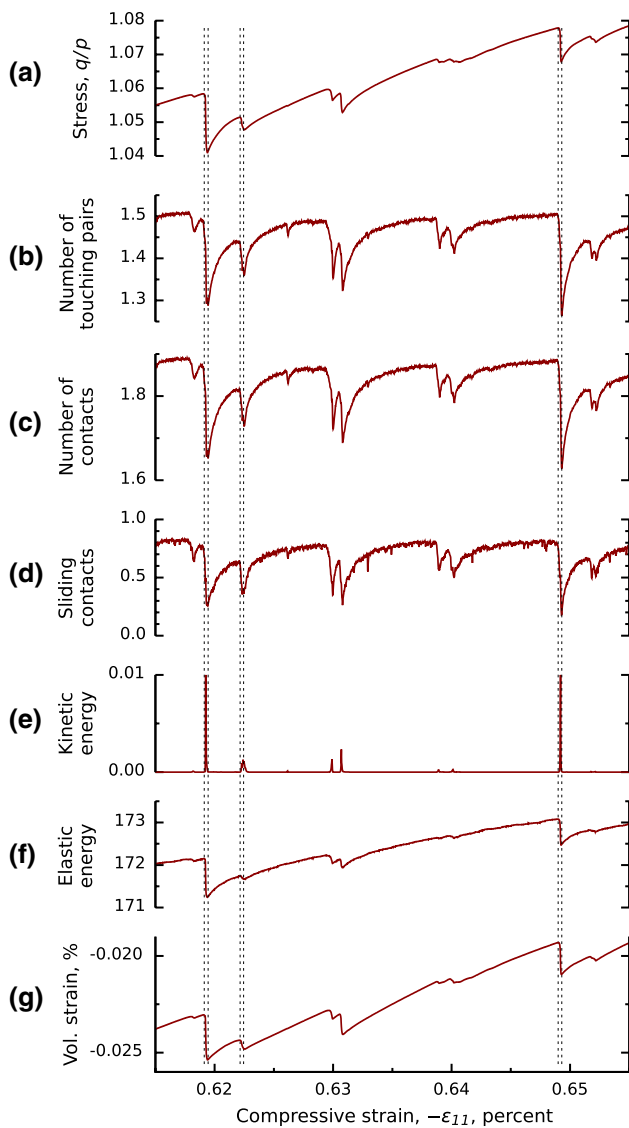


**Fig. 2** Details of stress and other characteristics during a small interval of strain, showing multiple stress-drops: **a** deviator stress; **b** number of touching particle-pairs divided by the number of particles; **c** number of contacts divided by the number of particles; **d** number of sliding contacts; **e** kinetic energy per unit volume,  $\text{N/m}^2$ ; **f** elastic contact energy per unit volume,  $\text{N/m}^2$ ; and **g** volume strain relative to the unloaded assembly

stress-recovery, the stiffness (slope) progressively decreases until the next stress-drop occurs.

Between the strains of 0 and 16%, more than 8200 stress-drops (and stress-recoveries) had occurred (Table 1). For this range of strains, the accumulated strain spent within these brief stress-drop periods accounted for a total strain of 0.22%, which accounts for about a seventh (14%) of the entire 16% range of strain. The remaining 86% of the 16% of strain was largely occupied in recovering from these drops in stress. In essence, at strains beyond 0.5%, deformation was largely filled by periods of rapidly declining stress and by

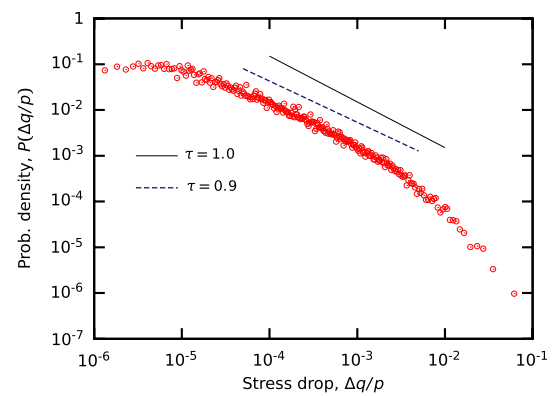


**Fig. 3** Probability density of stress-drop magnitudes,  $\Delta q/p$ , where  $\Delta q$  is the drop in the deviator stress  $\sigma_{11} - \sigma_{33}$  (the difference in stress in loading and lateral directions), normalized by dividing by the pressure (negative mean stress)

periods of recovery from these stress-drops. Prior to the final strain of 16%, the sum of all reductions in deviator stress  $q$  during the stress-drop episodes was over 1400 kPa. If only the stress-recoveries had occurred without their corresponding stress-drops, the deviator stresses would have reached a strength almost 10 times greater than the actual strength of 166 kPa. In this sense, stress-drops moderate granular strength and possibly reduce the amount of particle breakage that would occur if the increase in stress was unchecked.

Combe and Roux [30] conducted *stress*-controlled simulations, and they noted similar behavior to that of our strain-controlled conditions, but rather than exhibiting a brief drop in stress, they observed that stress would periodically stall and then rise again through strain hardening. Combe and Roux characterized this repeating pattern as a “Devil’s staircase.” Perhaps the strain-controlled behavior in Fig. 2 could be called a “Sisyphus ramp.”

We sought evidence of a periodicity or regularity of the lags between stress-drop events, but auto-correlation revealed no such pattern, and the stress-drops appeared to occur in a random, thoroughly irregular manner. After the first 1% of strain, stress-drops occurred at an average rate of roughly 5 drops per particle per unit (100%) of strain (Table 1). Figure 3 shows the probability density of the magnitude of the drops in deviator stress. The mean drop in deviator stress  $\langle \Delta q/p \rangle$  was greater than 170 Pa, but we also recorded several drops greater than 5 kPa, with the most severe being 10.2 kPa. The log-distribution has the greatest density at 20 Pa, roughly 0.02% of the mean stress. The mean stress in our constant- $p$  simulation was controlled with a servo-algorithm that maintained the mean stress to less than 0.01 Pa of the 100 kPa mean stress, and the left-most part of the distribution in Fig. 3 is likely influenced by this limit in resolution. The stress-drops that occur in plastic avalanches of amorphous solids have been analyzed

in a continuum (mean-field) framework by assuming that a material region has weak spots that remain stuck until activated by a local stress that exceeds a strength threshold, and once activated, stress is redistributed to other, possibly vulnerable, weak spots (see [31, 32]). This mean-field theory leads to a proportional scaling of the probability density, as  $P(\Delta q) \propto (\Delta q)^{-\tau}$ , with the mean-field exponent  $\tau = 1.5$ . Exponents in the range 1.2–1.5 have been observed in experiments and atomistic simulations of amorphous solids [28, 33–35] and with certain granular systems [6]. Our results from the loading of a densely compacted granular material are quite different, as the exponent  $\tau$  in Fig. 3 is between 0.9 and 1.0 for the broadest range of drop magnitudes.

Figure 2b, c, d show that each stress-drop is accompanied by a reduction in the numbers of total contacts and in the numbers of sliding contacts, and that the subsequent stress-recovery period coincides with a general increase in the numbers of contacts and sliding contacts. Because each particle is non-convex and can have multiple contacts with a neighboring particle, we make a distinction between the number of touching particle-pairs (Fig. 2b) and the total number of contacts (Fig. 2c). Note that both numbers have been divided by the number of particles in the assembly (10,648 sphere-clusters). The brief loss of contacts during stress-drop events is quite large, typically 10–20% of the number of particles (1000–2000 contacts among the 10,648 non-convex sphere-cluster particles, for which pairs of particles can share multiple contacts). Thornton [9] had also noted wide fluctuations in the number of contacts, and these results demonstrate that a stress-drop coincides with a substantial rearrangement, breaking, and disruption of the contact network, and that the subsequent recovery establishes a temporary stable network with more contacts.

Figure 2d, e show that each stress-drop is also accompanied by a spike in the cumulative kinetic energy of the particles and by a reduction in the elastic energy stored among the contacts (the micro-scale computation of the two energies is described in “Appendix” section). Peters and Walizer [8] also found that stress-drops were accompanied by bursts in the kinetic energy of the particles, fed by reductions in the elastic energy at the contacts, and Michlmayr et al. [11, 36] found that this kinetic energy is associated with low-frequency (0–20 kHz) acoustic energy emissions. Reductions in internal energy have also been observed in atomistic simulations of amorphous solids [19]. The increase in kinetic energy in our simulations reveals an intense activity of particles during stress-drops, an activity that has been associated with negative second-order work within the contacts [15, 24]. Indeed, elastic energy is, in part, transferred to kinetic energy, but this transfer to kinetic energy is a minor destination of the lost elastic energy. The change in elastic energy results primarily from a large but brief increase in frictional dissipation that greatly exceeds the smaller increase in

stress-work,  $\int \sigma_{ij} d\epsilon_{ij}$ . Changes in energy during the third stress-drop in Fig. 2 are summarized in Table 2. The changes per unit of volume have been normalized by dividing by the mean stress  $p$  of 100kPa and by the elapsed strain  $|\Delta\epsilon_{11}|$  of the drop. The sudden burst of kinetic energy is seen to be a minor destination of the work input. We also found that the increase in stress-work is predominately produced by a brief reduction in volume, as the volumetric work increment  $\frac{1}{3} \int \sigma_{ii} d\epsilon_{ij}$  (i.e., compare Fig. 2d, e, f). For the drained, constant pressure conditions of our simulations, each stress-drop is accompanied by an abrupt reduction in the assembly’s volume, evidence of a local collapse in the grain arrangement. Sudden reductions in granular volume were also noted by Cui et al. [7]. Such results differ from those of amorphous, glassy metals in which stress-drops are accompanied by volume coalescing and growth at a nano-scale [37].

## 2.2 Micro-scale origins of stress-drops

These bulk measurements indicate that stress-drops (and stress-recoveries) play an essential role in advancing the macro-scale stress during strain-hardening and failure, which raises the question: what micro-scale mechanisms are responsible for these stress-drops? Answering this question is necessary for understanding the micro-failure processes that limit strength and produce bulk failure within granular materials. To this end, we analyzed 3D spatial plots of several particle-scale characteristics for each of the three stress-drops identified in Fig. 2, and for three stress-drops that were isolated in similar simulations with linear-frictional contacts:

1. To determine whether a stress-drop is a diffuse weakening of material throughout the assembly or is a localized weakening within smaller regions of particles, we plotted the locations and magnitudes of particle velocities during each of the six stress-drops. Only load-bearing (non-rattler) particles were plotted, and the mean-field movement was first subtracted, to obtain velocities relative to the affine background movement.

**Table 2** Energy changes during the third stress-drop in Fig. 2

Type	Normalized change
Stress-work, $\sigma_{ij} \Delta\epsilon_{ij}$	5.5
Elastic energy	– 3.4
Frictional dissipation	8.8
Kinetic energy	0.1

Energy balance requires that  $\sigma_{ij} \Delta\epsilon_{ij}$  equal the sum of changes in elastic and kinetic energies and dissipation



2. Because stress-drops are brief periods of contact softening characterized by negative second-order work [14, 15], we located all contacts that were undergoing negative second-order work, where a contact's second-order work was computed as the inner product of the changes in its force  $\mathbf{f}$  and its movement  $\mathbf{u}$ , as  $\Delta \mathbf{f} \cdot \Delta \mathbf{u}$ . The locations of contacts with negative values and the magnitudes of these second-order values were plotted for instances before, during, and after each stress drop. With these plots, combined with the velocity plots, we could locate regions of the most intense activity and weakening within the assembly.
3. Stress-drops are accompanied by an increase in frictional dissipation (evident in Fig. 2e), so we also plotted the spatial distribution of dissipation.
4. A process called “force-chain buckling” has been hypothesized as the failure mechanism that limits granular strength in two-dimensional materials [38–40]. A force-chain is a sequence of particles connected by contacts that are part of the “strong contact” network: contacts with magnitudes of force greater than the mean contact force. Using methods described in [41], we identified the force-chains in our 3D assembly by computing the harmonic mean of the contact forces within the chains of contacts between each pair of load-bearing particles (about 35 million harmonic means, one for each particle-pair). To determine the relationship between force-chains and stress-drops, we focused on those particle-pairs within heavily loaded five-particle chains and plotted the most active of these heavily loaded particles during the six stress-drop events.
5. As will be seen, force-chain buckling was not a convincing source of the three stress-drops in Fig. 2, and we investigated another candidate mechanism: contact sliding that might eject (or “squirt”) a particle from its immediate neighbors. We plotted the potential locations and magnitudes of this mechanism.

For each of the three stress-drop episodes that are identified in Fig. 2, plots of particle velocities revealed a single region of 300–400 highly active particles whose velocity magnitudes were much greater than those among particles in the remainder of the assembly. The region of high activity was in a different location for each of the stress-drop episodes, but we have re-centered the periodic boundaries so that the region of high activity is centered within the assembly. These isolated regions encompassed only about 3% of the total assembly volume. Figure 4a is a plot of velocity magnitudes for the third stress-drop in Fig. 2, with each sphere representing a single particle, and its average velocity is measured during the brief 0.002% strain that elapsed during the drop. A sphere's diameter is proportional to the logarithm of the particle's speed (recall that the particles are themselves

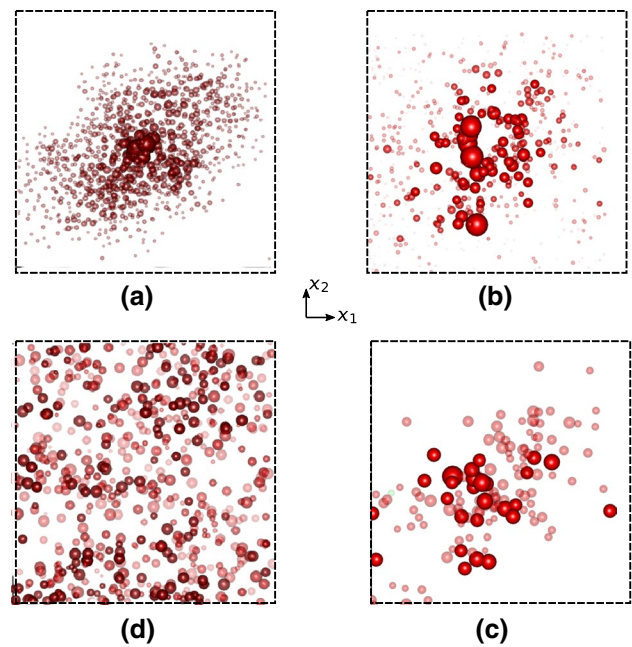


**Fig. 4** Spatial plots of internal activity during the third stress-drop that is identified in Fig. 2. Each sphere represents a single sphere-cluster particle (subfigures a, c, and d) or a single contact (subfigure b), and the sphere's diameter is proportional to the logarithm of activity: **a** logarithm of particles' speeds; **b** logarithm of negative second-order work in the contacts; **c** logarithm of changes in the most heavily loaded force-chains, with opacity also proportional to the logarithm of change; and **d** logarithm of contact slip dissipation for those particles with three or more slipping contacts

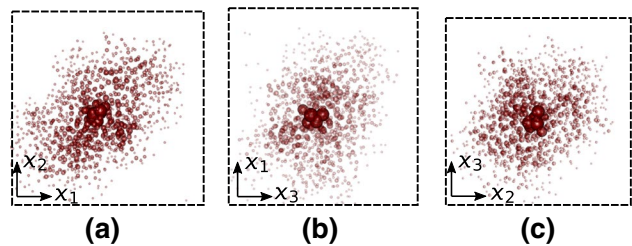


**Fig. 5** Spatial plots of particle speeds in three planes for the third stress-drop in Fig. 2: **a**  $x_1 - x_2$  plane, which repeats Fig. 4a; **b**  $x_3 - x_1$  plane; and **c**  $x_2 - x_3$  plane. Each sphere represents a particle, and a sphere's diameter and opacity is proportional to the particle's speed

not spheres, but are non-convex sphere-clusters). The plot is a projection of the particles' positions onto the  $x_1 - x_2$  plane, noting that triaxial compression occurs in the  $x_1$  (horizontal) direction. Fig. 4a shows that particle activity is not diffuse and uniform during a stress-drop; rather, intense movement is localized within a small neighborhood of particles. The local nature of activity is emphasized with Fig. 5, which repeats the Fig. 4a of particle velocities but also shows projections in the  $x_3 - x_1$  and  $x_2 - x_3$  planes. Again, only a small region of activity is responsible for the stress-drop, and for

this reason we resist the use of “avalanche” to characterize stress-drops in granular materials, a term that is commonly used with amorphous solids to describe an accumulation or cascading of atomic-scale events that lead to bulk plasticity [42].

Returning to the previous figure, Fig. 4b shows the locations of contacts actively undergoing negative second-order work (contact softening) during the same stress-drop. The spheres in this figure represent individual *contacts*, and the spheres’ diameters are proportional to the logarithms of the contacts’ negative second-order work rates. Although about 800 contacts exhibited negative second-order work during this stress-drop, the figure only shows the 100 contacts with the greatest magnitudes (to more clearly identify those contacts with the largest magnitudes of negative second-order work, the opacity has been reduced for the other contacts). Contacts with large magnitudes are located throughout the assembly, but the contacts with the largest magnitudes of second-order work are concentrated within the same region in which the particle velocities were largest (compare Fig. 4a, b). A similar coincidence was found for the other stress-drops, although the most active contacts were located in a different region of the assembly for each of the three stress-drops. We conclude that movement and failure are spatially and temporally coincident and are localized within a small volume of material.

In addition to Fig. 4a, b, we also plotted the spatial distribution of frictional dissipation at contacts within the assembly. Although contact sliding occurred throughout the assembly, dissipation—the product of the contact sliding rates and the tangential forces—was more intense in the same regions having large particle velocities and large negative second-order work (i.e., the active regions in Fig. 4a, b).

For the loading periods immediately before and after a stress-drop, we could also find particles with large kinetic energy and contacts with significant second-order work, but the spatial distribution of these two characteristics was diffuse, unlike that during the stress-drop, and any modest spatial concentration before and after a stress-drop occurred in regions other than those observed during the stress-drop. We were surprised that the number of contacts undergoing negative second-order work during a stress-drop was typically *smaller* than the numbers immediately before or after the stress-drop, and fewer contacts were sliding during a stress-drop than before or after (see Fig. 2c). Although a smaller number of contacts was involved, the intensity of sliding and of negative second-order work among contacts was much greater during the stress-drops, another indication that intense movement and failure are limited to a small number of contacts.

We searched for a causative mechanism of the three stress-drops in Fig. 2. We began by looking for a spatial

correlation between *force-chain activity* and the failure regions of 300–400 particles in which velocity, dissipation, and negative second-order work were concentrated. Particular attention was placed upon *changes* in the force-chains that were occurring during the initial stage of a stress-drop, as such changes would indicate a causative relation between force-chain activity and a stress-drop. As described above and in [41], force-chains were identified by computing the harmonic means of the contact forces within every chain of five particles. We identified the 20% of chains having the largest mean harmonic force and then further isolated the 20% of these chains that had experienced the greatest change in mean harmonic force during the initial stage of a stress-drop. This selection process produced a list of the most active and heavily loaded force-chains (a list of about 12,000 five-particle chains). Of course, a single particle can belong to many different particle-chains, since each of our chains was composed of five particles. To identify the particles most acutely involved in a stress-drop—the “pivotal particles” within the force-chain network—we counted the number of chains associated with each particle (some particles were at the intersection of more than 100 heavily loaded and rapidly changing five-particle chains). These pivotal particles are plotted in Fig. 4c for the third stress drop in Fig. 2. Each sphere represents a particle and the diameter is roughly equal to the particle’s size. A sphere’s opacity is proportional to the logarithm of the number of chains with which it was associated, with most particles being nearly transparent.

Consistent with the results of other investigators, more force-chain activity occurs during a stress-drop than during the periods before and after a stress-drop [43]. The opaque, pivotal particles in Fig. 4c belong to those heavily-loaded force-chains that are undergoing the largest changes in force during the initial stage of the stress-drop. Although some of these particles are arranged as clusters and chains, they are diffusely located throughout the assembly and are not concentrated within or in the immediate vicinity of the failure region seen in Fig. 4a, b. This result, which was common to the three stress-drops that we investigated, suggests that stress-drops are not triggered by a collapse (buckling) of the force-chain network. Force-chain activity is coincident with and the consequence of stress-drops, but it is unlikely their cause. Rather, changes within force-chains are caused by of some other triggering mechanism, a mechanism that likely occurs within the localized failure region where particle velocities are large, frictional dissipation is intense, and negative second-order work is common and acute. A brief reduction in deviator stress—a stress-drop—results, of course, from reductions in the contact forces, and these reductions occur primarily within force-chains. However, the stress-drops that we investigated were likely triggered by another mechanism. This conclusion is supported by other evidence. The sudden small reduction in assembly volume

and the brief increase in frictional dissipation (Fig. 2e, f) suggest a kinematic mechanism that involves intense sliding and produces a brief but localized collapse (akin to a small implosion) of the internal particle arrangement.

One such mechanism is illustrated in Fig. 6a for a system of three disks. Suppose that the upper and lower particles are restrained from rotating while they are progressively compressed against the middle particle. Although the two contacts are initially compressed in an elastic manner as  $P$  increases, when the friction limit is reached at the contacts (i.e., when angle  $\theta \geq \tan^{-1} \mu$ ), the system can not support a sustained load  $P$ , and accelerated sliding and negative second-order work ensue: the system becomes unstable,  $P$  is reduced, and the middle particle is “squirted” to the right. We hypothesize that a stress-drop is produced when multiple contacts around a particle reach the frictional limit and the particle is dislodged from its neighborhood of particles. This mechanism would produce rapid changes in the angles  $\theta$  similar to the “buckling” definition of Tordesillas et al.

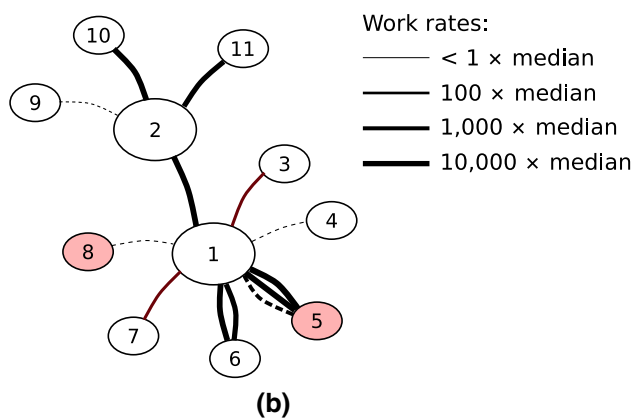
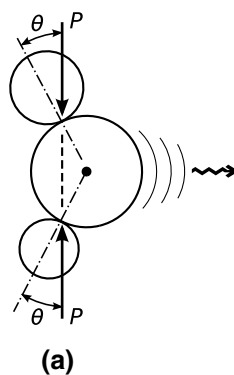


**Fig. 6** **a** Proposed mechanism of local instability, with the middle particle squirted to the right. **b** Contact topology of two rapidly moving particles during the stress-drop of Fig. 4 (the third stress-drop in Fig. 2). Solid lines represent slipping contacts; dashed lines are non-slipping contacts. Line width represents a contact’s work rate relative to the assembly’s median rate. Red lines designate contacts that are not undergoing negative second-order work

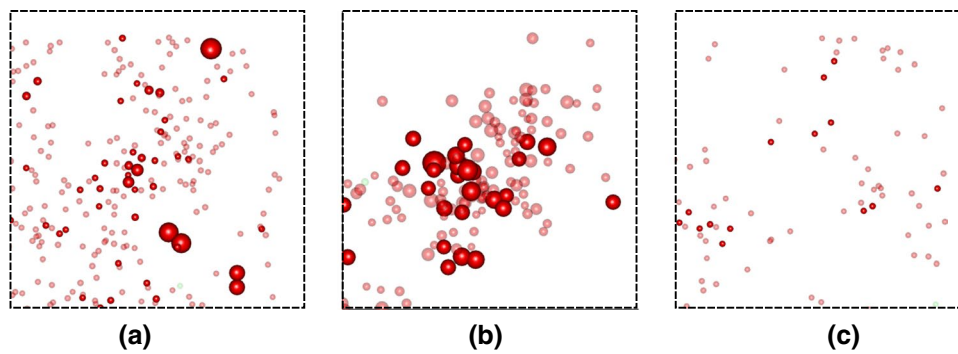
[40], but the current focus is on the sliding of the particles rather than the changes in angle—changes that can also be produced by rolling or by the rigid rotation of particle pairs [44].

Figure 4d depicts the sliding velocities of particles that have multiple slipping contacts. The figure is taken during the third of the stress-drops identified in Fig. 2. Each sphere in Fig. 4d represents a particle with two or more slipping contacts, and its diameter and opacity is proportional to the logarithm of the sum of the dissipation rates at the particle’s contacts (i.e., the inner product of contact force and contact movement). A small cluster of such active particles is located within the failure region of intense particle activity and negative second-order work (cf. Fig. 4a, b). The same situation existed for the other stress-drops that we investigated: at the start of and during a stress-drop, a few particles, located within the failure region, had multiple rapidly slipping contacts. Similar plots taken immediately before and after a stress-drop are shown in Fig. 7. These plots show no intense activity either before (Fig. 7a) or after (Fig. 7c) the stress-drop had occurred within the active, failure region. These observations suggest that stress-drops are produced abruptly when multiple contacts around one or more pivotal particles slip, leading to the local instability of a group of particles and a reduction in their contact forces. A stress-drop likely comes to an end when new contacts are formed, such that the unstable particles become newly buttressed within a rearranged system of contacts.

An example of the contact topology of rapidly moving particles is depicted in Fig. 6b. The two particles, labeled 1 and 2, are the most active during the third stress-drop that is highlighted in Fig. 4, with both particles represented by the largest spheres in Fig. 4d. The contacting neighborhood of the two particles includes nine other particles: particle 1 touches particles 2–8, and particle 2 touches particle 1 and particles 9–11. Because the particles are non-convex, some neighboring particles have multiple contacts. Only two of the eleven particles are among the “strong contact” network (i.e., particles with a larger-than-average mean stress [45]), identified as the shaded particles 5 and 8 in Fig. 6b); whereas, all other particles are within the weak network of modestly loaded particles. In the figure, solid lines represent slipping contacts; dashed lines are non-slipping contacts. Both particles 1 and 2 have multiple slipping contacts, and the magnitudes of contact slip are quite large, as the thicknesses of the lines represent the contact work rates relative to the median value of all contacts in the assembly. The work rates of the slipping contacts around these two pivotal particles was several orders of magnitude larger than the median rate.

Of the nine slipping contacts in Fig. 6b, seven were undergoing negative second-order work, which is akin to the situation depicted in Fig. 6a (the two contacts not





**Fig. 7** Spatial plots of contact slip dissipation for the third stress-drop that is identified in Fig. 2. The sub-figures show dissipation **a** immediately before, **b** during, and **c** immediately after the stress-drop. Subfigure (b) is the same as Fig. 4d. In each subfigure, a sphere repre-

sents a single sphere-cluster particle and the sphere's diameter is proportional to the contacts slip dissipation for those particles with three or more slipping contacts

undergoing second-order work are 1–4 and 1–7, designated with red lines). We identified a similar situation in all of the stress-drops that we investigated: one or two particles within the localized failure zone had multiple slipping contacts with movement rates of more than a hundred times the median rate and exhibited large negative second-order work. The simultaneous slipping of multiple contacts around one or two pivotal particles, such as the “squirted” particle in Fig. 6a, is a credible causative condition of our stress drops.

### 3 Effects of contact model, particle shape, mean stress, and assembly size

The simulation results of the previous section were for a large dense assembly of sphere-cluster particles having Cattaneo–Mindlin contacts and compacted to an initial pressure of 100 kPa. Table 3 gives results for simulations that differ in various respects from the previous simulation.

All of the simulations were of triaxial constant- $p$  loading conditions, and column 2 gives results for the base-case of Sect. 2. The table reports statistics on the drop in deviator stress and the change in volume during stress-drop events that had occurred during the medium-strain range of 2–10% strain. In addition to mean values, the table also give values for the 2% of most severe drops (the 98th percentile values). These results indicate the following:

- Column 3 gives results for an assembly that was compacted to a smaller 10 kPa mean stress, a tenth of the base-case. Although the drops in deviator stress are smaller than for the 100 kPa base-case (column 2), the drops are a greater fraction of the compaction stress, indicating that stress-drops are relatively more severe for lower confinement stress. Note, however, that stress-drops are less frequent and produce smaller reductions in volume than with a 100 kPa confinement stress.
- Column 4 gives results of sphere-cluster particles with a simple linear–frictional contact model, simpler than the

**Table 3** Comparison of stress-drops for different particle shapes, contact models, confinement stresses, and densities. All statistics are for the range 2–10% of strain

(1) Measure	(2) Clusters C–M contact <sup>a</sup> 100 kPa dense	(3) Clusters C–M contact <sup>a</sup> 10 kPa dense	(4) Clusters L–F contact <sup>a</sup> 100 kPa dense	(5) Spheres L–F contact <sup>a</sup> 100 kPa dense	(6) Spheres L–F contact <sup>a</sup> 100 kPa medium	(7) Spheres C–M contact <sup>a</sup> 100 kPa dense
Mean stress-drop $\langle \Delta q \rangle$	167 Pa	27 Pa	141 Pa	247 Pa	263 Pa	213 Pa
98 pctl. stress-drop	1520 Pa	240 Pa	1300 Pa	1770 Pa	2060 Pa	1580 Pa
Mean volume strain	$-3.0 \times 10^{-6}$	$-1.5 \times 10^{-6}$	$-2.3 \times 10^{-6}$	$-3.6 \times 10^{-6}$	$-3.9 \times 10^{-6}$	$-0.6 \times 10^{-6}$
98 pctl. volume strain	$-4.8 \times 10^{-5}$	$-3.2 \times 10^{-5}$	$-3.5 \times 10^{-5}$	$-6.1 \times 10^{-6}$	$-3.0 \times 10^{-5}$	$-2.6 \times 10^{-5}$
Rate of drops <sup>b</sup>	5.0	2.6	4.6	10.9	12.5	4.3

<sup>a</sup>C–M = Cattaneo–Mindlin contact; L–F = linear–frictional contact

<sup>b</sup>Number of drops per 1% strain per particle

Cattaneo–Mindlin model of column 2. The results for the two contact models are quite similar, although the linear–frictional model produces somewhat less severe and less frequent stress and volume drops. A similar result is also seen for sphere particles, by comparing columns 6 and 7, with linear–frictional and Cattaneo–Mindlin contacts, respectively.

- Column 5 is for sphere particles and shows that drops in deviator stress are much larger and are more frequent for spheres than for non-convex sphere-cluster particles (i.e., compared with column 4). A similar result is seen by comparing the sphere results in column 7 with the clusters of column 2.
- By comparing column 5 of a dense assembly of spheres with column 6 for a medium-to-loose assembly, we see that drops in stress and reductions in volume are somewhat greater for the medium assembly. The dense and medium assemblies had void ratios of 0.534 and 0.692, respectively.

To investigate the influence of assembly size on the severity of stress-drops, we analyzed a data-set that had been co-prepared by the first author for a series of two-dimensional simulations of disk assemblies [3]. In that study, multiple assemblies with 64, 256, 1024, 4096, and 10,816 disks were loaded in biaxial compression, and as with the three-dimensional simulations of the current work, plots of stress and strain revealed an irregular repetition of stress-drop events of various magnitudes. The results are summarized in Fig. 8, which shows the mean change of deviator stress,  $\langle \Delta q/p \rangle$ , for the five assembly sizes, with the deviator stress normalized by dividing by the mean stress. As would be expected, the average severity of the stress-drops is reduced with an increase in assembly size, although the magnitudes of the drops are larger than those for three-dimensional assemblies. The reduction with size does not occur in a linear manner; rather, the average drop in deviator stress is roughly

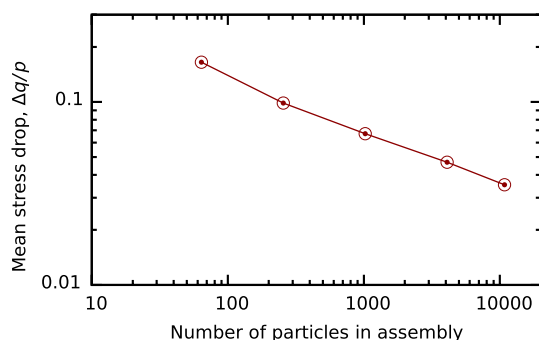


**Fig. 8** Affect of assembly size on the mean drop in deviator stress for two-dimensional disk assemblies (after [3]) The stress-drops are normalized by dividing by the confining pressure  $p$

proportional to assembly size (i.e. numbers of particles) raised to the power of  $-0.294$ :  $\text{mean}(\Delta q/p) \approx 0.533N^{-0.294}$ , where  $N$  is the number of disks in an assembly. This result is similar to that of amorphous solids, for which atomistic simulations demonstrate that the mean stress-drop decreases with increasing specimen size, but with a quite different exponent: in keeping with the theory of Karmakar [46] that predicts an exponent of  $-2/3$ , the atomistic simulations yield exponents in the range  $-0.61$  to  $-0.7$  [17, 18, 47].

Finally, we also investigated the occurrence of stress-drops during purely isotropic loading. An assembly of spheres with Cattaneo–Mindlin contacts was isotropically consolidated at a constant rate of volumetric compression from a mean stress of 5.8–100 kPa. No sudden drops occurred in the mean stress  $p$ , and only three small changes in the deviator stress occurred in the course of the 0.26% reduction of volume. We conclude that the stress-drops in our simulations of resilient, non-breaking particles are induced by deviatoric (not volumetric) deformation.

## 4 Conclusions

Micro-scale movements and forces within a granular material are known to be irregular and complex. Individual particles move in an erratic and desultory manner; the forces at individual contacts tack and turn in seemingly capricious ways; and deviations from mean trends—of particle rotations, of local strains, of individual contact forces, etc.—are surprisingly large [41]. Yet from this micro-scale tumult, a greater order is expressed at the meso- and bulk scales. For example, contact forces are organized into meso-scale force-chains, movements are coordinated in vorticity patterns that encompass hundreds of particles, and strains are shaped into micro-bands and other meso-scale features. The bulk behavior is even more regular, and simple constitutive forms can capture the primary trends of the stress-strain behavior and can even predict the onset of localization and failure. Even so, when one looks closely at the results of laboratory tests and of discrete simulations, the irregularities produced by the micro-scale ferment can be recognized, and significant deviations from simple constitutive descriptions are seen.

Substantial deviations from standard continuum models are expressed in abrupt irregularities in the stress-strain response. Notably, deformation during strain-hardening and failure is distinguished by frequent but irregular drops of stress. With small specimens, such of those of our (and most other) simulations, these stress-drops obscure the general stress-strain trend and obscure the characterization of bulk stiffness and strength characteristics. We found that the average frequency of stress-drops was about 5 drops per particle per unit (100%) of strain. Moreover, a stress-drop is not occasioned by the general instability of

an entire assembly, but is instead focused within a small cluster of a few hundreds of particles. To place these values in perspective, a conventional engineering test to determine the strength of a sand specimen with particles of, say, 1 mm size will contain several hundreds of thousands of particles, and if we assume that the frequency of drops is, say, proportional to number of particles, then the spacing of the stress-drops in a sand specimen, each with a strain duration of  $2 \times 10^{-6}$ , would occur at strain intervals of, say,  $1 \times 10^{-6}$ , usually overlapping other stress-drops. When scaled from the results of our simulations, the average magnitude of a stress-drop for the laboratory specimen would be much less than the mean 170 Pa drop in stress of our simulations, and because of their rapidity and small magnitude, multiple drops would occur simultaneously in the sand specimen and all but the largest stress-drops would likely go unnoticed during a conventional laboratory test. Nonetheless, for laboratory specimens as well as in our simulations, granular deformation is largely occupied in a sequence of stress-drops and of recoveries from these drops—a Sisyphus ramp toward eventual bulk failure. We also note that stress-drops much larger than those in our simulations have been observed in experiments with glass and plastic beads [2, 7, 11] and have been attributed to stick-slip. Our simulations employed a rate-independent contact mechanism, and the stress-drops result from rate-independent slip between particles.

A stress-drop is occasioned by large changes in the numbers of contacts and in the numbers of sliding contacts, indicating significant alterations of the particles' arrangement. The most rapid particle motions during a drop are confined, however, to a cluster of a few hundreds of particles. Each rearrangement of a cluster produces a reduction in volume, as a local and momentary implosion of the assembly that can briefly counter the prevailing trend of dilation occurring elsewhere in the specimen. The underlying mechanism of a stress-drop seems to be the sudden sliding of multiple contacts around a single culpable particle or cluster of particles, producing local rates of contact sliding, dissipation, and negative second-order work (i.e. contact softening) that are hundreds or thousands of times larger than the median rate.

Extensive attention has been given the similar phenomenon of avalanches (i.e. plastic episodes) in amorphous solids. Our results reveal notable differences with granular stress-drops: a different scaling of drop magnitude and frequency, a different scaling of drop magnitude and assembly size, and the spatially isolated, non-cascading character of granular stress-drops.

## Compliance with ethical standards

**Conflict of interest** The authors declare that they have no conflict of interest.

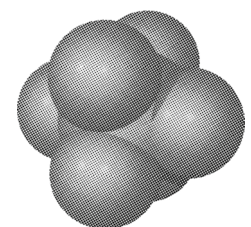
## DEM modeling details

Discrete element simulations were conducted with a cubical assembly of 10,648 particles contained within periodic boundaries. The simulations were intended to produce a modest fidelity to the bulk behavior of sands at low confining stress. Because sphere assemblies produce unrealistic rolling between particles and have a low bulk strength, we used a bumpy, non-convex cluster shape for the particles: a large central sphere with six smaller embedded outer spheres in an octahedral arrangement (Fig. 9). The use of non-spherical particles circumvents the need of artificial measures to restrain the particle rotation (for example, the use of rotational contact springs or the direct restraint of particle rotations, as in [48, 49]). Through trial and error, we chose the radii of the central and outer spheres so that the bulk behavior approximated that of Nevada Sand, a standard poorly graded sand (SP) use in laboratory and centrifuge testing programs [22, 23]. The particle size range was 0.074–0.28 mm, with  $D_{50} = 0.165$  mm.

To create assemblies with a range of densities, we began with the particles sparsely and randomly arranged within a cubic periodic cell. With an initial low inter-particle friction coefficient ( $\mu = 0.20$ ), the assembly was isotropically reduced in dimension until it “seized” when a sufficiently complete contact network had formed. A series of 25 progressively denser assemblies were created by repeatedly assigning random velocities to the particles of the previous assembly and then further reducing the cell's dimensions until it, too, had seized. The 25 assemblies had void ratios ranging from 0.781 to 0.586 (solid fractions of 0.561 to 0.664). The single assembly used in the paper had void ratio 0.690 (solid fraction 0.592) and approximates the behavior of Nevada Sand at a relative density of 40%. After compaction, the assembly was allowed to quiesce with friction coefficient  $\mu = 0.40$ , which was then raised to  $\mu = 0.55$  for the subsequent loading simulations.

The particles are durable (non-breaking) and interact only at their contacts. A Hertz, Cattaneo–Mindlin contact model was used in the simulations. The model is a full implementation of a Hertz–Mindlin contact between elastic–frictional bodies. We used the Jäger algorithm, which can model arbitrary sequences of normal and tangential contact movements

Fig. 9 Sphere-cluster particle



[21]. With the Cattaneo–Mindlin contacts, the loading simulations were conducted with an inter-particle friction coefficient  $\mu = 0.55$ , particle shear modulus  $G = 29$  GPa, and Poisson ratio  $\nu = 0.15$ . The contact model is rate-independent, such that the contact force depends upon the movement history and not on the particles’ velocities. A special servo-algorithm was used for precisely maintaining constant mean stress during the constant- $p$  simulations [50]. Because the shear modulus was much greater than the mean stress of 100 kPa, the contacts were relatively stiff, and the average overlap at a contact was about 0.1% of the particle diameter.

In Fig. 2d, e, we show the kinetic and elastic energies per unit of bulk volume. The energies were derived from an energy-audit of the assembly: the increment of stress-work,  $\int \sigma_{ij} d\epsilon_{ij}$ , during an increment of strain must equal the sum of the volume-averages of the change in elastic energy within the contacts, the frictional dissipation at the contacts, and the change in the particles’ kinetic energy. By directly computing the stress-work, the elastic energy, and the frictional dissipation, as described below, we could find the change in the kinetic energy. The kinetic energy was also independently computed from the particles’ velocities and masses, and we found that the two values almost exactly matched, thus verifying the energy balance.

The stress-work was computed in the usual manner from bulk measures of stress and strain (the former was computed from the contact forces and branch vectors by using the usual Navier–Love–Rothenburg equation; whereas, the strain was computed from the boundary displacements). Contact elastic energy was computed as the sum of normal and tangential parts. In conventional simulations, contacts are assumed to occur between spherical surfaces, but this approach leads to a bulk small-strain stiffness that increases with the means stress  $p$  as  $p^{1/3}$ . In our simulations, we allowed for non-spherical contours (asperities) at the contacts, as this approach yielded a small-strain modulus that was proportional to the mean stress  $p$  raised to the power of 0.5, a common observation in geotechnical practice (see [22] for details). We used a power-law type ( $z = A_\alpha r^\alpha$ ) of contact profile as described by Jäger [51] with a profile parameter  $\alpha = 1.3$ . The normal elastic energy  $E_n$  in a single contact is given as

$$E_n = \frac{4\alpha^2 G a \zeta^2}{(1 + 2\alpha)(1 + \alpha)(1 - \nu)} \tag{1}$$

where  $G$  and  $\nu$  are the shear modulus and Poisson ratio of the particles,  $\zeta$  is the contact indentation (one half of the overlap),  $a$  is the radius of the contact zone,

$$a = \left[ \frac{\zeta}{A_\alpha \sqrt{\pi}} \frac{\Gamma(\frac{\alpha+1}{2})}{\Gamma(\frac{\alpha+2}{2})} \right]^{1/\alpha} \tag{2}$$

and  $\Gamma(\cdot)$  is the gamma function (see [51]). Note that the normal part of elastic energy can be directly computed from the accumulated indentation of the contact. The tangential response, however, is history-dependent and must be computed in an incremental manner. For each time increment  $\Delta t$  in our DEM simulations with Cattaneo–Mindlin contacts, we computed the increment of elastic (reversible) tangential displacement  $\Delta \xi^{(r)}$  and subtracted this reversible increment from the full tangential increment  $\Delta \xi$  to find the irreversible, frictional tangential increment,

$$\Delta \xi^{(i)} = \Delta \xi - \Delta \xi^{(r)} \tag{3}$$

and then computed the inner product of the irreversible increment and the tangential force to find the increment of dissipation:

$$\text{Contact dissipation} = \mathbf{f}^t \cdot \Delta \xi^{(i)} \tag{4}$$

To find the incremental elastic (reversible) tangential movement  $\Delta \xi^{(r)}$  in Eq. (3), which represents the response to the increment of tangential force  $\Delta \mathbf{f}^t$  in the absence of micro-slip, we used Walton’s solution for the tangential contact response of rough (zero-slip) surfaces [52]:

$$\Delta \xi^{(r)} = \frac{2 - \nu}{8G} \frac{1}{a} \Delta \mathbf{f}^t \tag{5}$$

In this manner, we tracked the incremental frictional dissipation of each Cattaneo–Mindlin contact so that the total contact frictional dissipation, the total contact elastic energy, the stress-work, and the kinetic energy of the assembly could be computed in a consistent manner.

In conducting the simulations, we intended to model quasi-static, rate-independent behavior. To this end, we used a slow strain rate (strain increments of  $2 \times 10^{-9}$  and minimal viscous damping (2% of critical damping)). The inertial number  $I = \dot{\epsilon} \sqrt{m/(pd)}$ , a relative measure of loading and inertial rates, was about  $1 \times 10^{-11}$ , signifying nearly quasi-static loading [53]. During loading, the average imbalance of force on a particle was less than 0.003% of the average contact force (parameter  $\chi$  in [54, 55]). The average kinetic energy of the particles was less than  $3 \times 10^{-7}$  times the elastic energy in the contacts. With the very slow strain rates of the simulations, doubling the strain increment from  $1 \times 10^{-8}$  to  $2 \times 10^{-8}$  had minimal effect on the monotonic stress-strain response. Boundary movements were regulated so that any six of the stress or strain components (or any six linear combination of these components) could be controlled at desired rates. During the constant- $p$  (constant mean stress) triaxial loading, the mean stress would remain within 0.01 Pa of the 100 kPa target. All of these measurements indicate that the behavior in the simulations was nearly quasi-static and independent of loading rate.

The DEM simulations were done with the authors’ OVAL code (see [22]) and were run with a 4th generation Intel



i7 processor on a single thread. The monotonic loading in Fig. 1, in which the strain was advanced to 16%, took 60 days of compute time.

## References

- Roux, J.-N., Combe, G.: On the meaning and microscopic origins of quasistatic deformation of granular materials, In: Proceedings of the 16th ASCE Engineering Mechanics Conference, vol. 759, ASCE, pp. 1–5 (2003)
- Alshibli, K., Alramahi, B.: Microscopic evaluation of strain distribution in granular materials during shear. *J. Geotech. Geoenviron. Eng.* **132**(1), 80–91 (2006). [https://doi.org/10.1061/\(ASCE\)1090-0241\(2006\)132:1\(80\)](https://doi.org/10.1061/(ASCE)1090-0241(2006)132:1(80))
- Kuhn, M.R., Bagi, K.: Specimen size effect in discrete element simulations of granular assemblies. *J. Eng. Mech.* **135**(6), 485–492 (2009)
- Sun, W., Ostien, J.T., Salinger, A.G.: A stabilized assumed deformation gradient finite element formulation for strongly coupled poromechanical simulations at finite strain. *Int. J. Numer. Anal. Methods Geomech.* **37**(16), 2755–2788 (2013)
- Nicot, F., Hadda, N., Sibille, L., Radjai, F., Hicher, P.-Y., Darve, F.: Some micromechanical aspects of failure in granular materials based on second-order work. *Comptes Rendus Mécanique* **342**(3), 174–188 (2014)
- Denisov, D.V., Lörincz, K.A., Uhl, J.T., Dahmen, K.A., Schall, P.: Universality of slip avalanches in flowing granular matter. *Nat. Commun.* **7**, 10641 (2016)
- Cui, D., Wu, W., Xiang, W., Doanh, T., Chen, Q., Wang, S., Liu, Q., Wang, J.: Stick-slip behaviours of dry glass beads in triaxial compression. *Granul. Matter* **19**(1), 1 (2017)
- Peters, J.F., Walizer, L.E.: Patterned nonaffine motion in granular media. *J. Eng. Mech.* **139**(10), 1479–1490 (2013)
- Thornton, C.: Numerical simulations of deviatoric shear deformation of granular media. *Géotechnique* **50**(1), 43–53 (2000)
- Michlmayr, G., Cohen, D., Or, D.: Sources and characteristics of acoustic emissions from mechanically stressed geologic granular media—a review. *Earth Sci. Rev.* **112**(3), 97–114 (2012)
- Michlmayr, G., Cohen, D., Or, D.: Shear-induced force fluctuations and acoustic emissions in granular material. *J. Geophys. Res. Solid Earth* **118**(12), 6086–6098 (2013)
- Ingraham, M.D., Issen, K.A., Holcomb, D.J.: Use of acoustic emissions to investigate localization in high-porosity sandstone subjected to true triaxial stresses. *Acta Geotech.* **8**(6), 645–663 (2013)
- Daouadji, A., Hicher, P.Y., Jrad, M., Sukumaran, B., Belouettar, S.: Experimental and numerical investigation of diffuse instability in granular materials using a microstructural model under various loading paths. *Géotechnique* **63**(5), 368 (2013)
- Nicot, F., Daouadji, A., Hadda, N., Jrad, M., Darve, F.: Granular media failure along triaxial proportional strain path. *Eur. J. Environ. Civil Eng.* **17**(9), 777–790 (2013)
- Nguyen, H.N.G., Prunier, F., Djeran-Maigre, I., Nicot, F.: Kinetic energy and collapse of granular materials. *Granul. Matter* **18**(1), 1–10 (2016)
- Lerner, E., Procaccia, I.: Locality and nonlocality in elastoplastic responses of amorphous solids. *Phys. Rev. E* **79**(6), 066109 (2009)
- Hentschel, H.G.E., Karmakar, S., Lerner, E., Procaccia, I.: Size of plastic events in strained amorphous solids at finite temperatures. *Phys. Rev. Lett.* **104**(2), 025501 (2010)
- Dasgupta, R., Karmakar, S., Procaccia, I.: Universality of the plastic instability in strained amorphous solids. *Phys. Rev. Lett.* **108**(7), 075701 (2012)
- Zhang, D., Dahmen, K.A., Ostojca-Starzewski, M.: Scaling of slip avalanches in sheared amorphous materials based on large-scale atomistic simulations. *Phys. Rev. E* **95**(3), 032902 (2017)
- Daouadji, A., Darve, F., Al Gali, H., Hicher, P.Y., Laouafa, F., Lignon, S., Nicot, F., Nova, R., Pinheiro, M., Prunier, F., et al.: Diffuse failure in geomaterials: experiments, theory and modelling. *Int. J. Numer. Anal. Methods Geomech.* **35**(16), 1731–1773 (2011)
- Kuhn, M.R.: Implementation of the Jäger contact model for discrete element simulations. *Int. J. Numer. Methods Eng.* **88**(1), 66–82 (2011)
- Kuhn, M.R., Renken, H., Mixsell, A., Kramer, S.: Investigation of cyclic liquefaction with discrete element simulations. *J. Geotech. Geoenviron. Eng.* **140**(12), 04014075 (2014). [https://doi.org/10.1061/\(ASCE\)GT.1943-5606.0001181](https://doi.org/10.1061/(ASCE)GT.1943-5606.0001181)
- Arulmoli, K., Muraleetharan, K.K., Hossain, M.M., Fruth, L.S.: VELACS verification of liquefaction analyses by centrifuge studies laboratory testing program soil data report, Technical Report Project No. 90-0562, The Earth Technology Corporation, Irvine, CA, data available through <http://yees.usc.edu/velacs> (1992). Accessed 21 Dec 2011
- Sibille, L., Hadda, N., Nicot, F., Tordesillas, A., Darve, F.: Granular plasticity, a contribution from discrete mechanics. *J. Mech. Phys. Solids* **75**, 119–139 (2015)
- Laouafa, F., Prunier, F., Daouadji, A., Al Gali, H., Darve, F.: Stability in geomechanics, experimental and numerical analyses. *Int. J. Numer. Anal. Methods Geomech.* **35**(2), 112–139 (2011)
- Cabalar, A.F.: Stress fluctuations in granular material response during cyclic direct shear test. *Granul. Matter* **17**(4), 439–446 (2015)
- Roux, J.-N., Combe, G.: Quasistatic rheology and the origins of strain. *C. R. Phys.* **3**(2), 131–140 (2002)
- Lin, J., Lerner, E., Rosso, A., Wyart, M.: Scaling description of the yielding transition in soft amorphous solids at zero temperature. *Proc. Natl. Acad. Sci.* **111**(40), 14382–14387 (2014)
- Nicot, F., Hadda, N., Bourrier, F., Sibille, L., Wan, R., Darve, F.: Inertia effects as a possible missing link between micro and macro second-order work in granular media. *Int. J. Solids Struct.* **49**(10), 1252–1258 (2012)
- Combe, G., Roux, J.-N.: Strain versus stress in a model granular material: a devil's staircase. *Phys. Rev. Lett.* **85**(17), 3628–3631 (2000)
- Dahmen, K.A., Ben-Zion, Y., Uhl, J.T.: Micromechanical model for deformation in solids with universal predictions for stress-strain curves and slip avalanches. *Phys. Rev. Lett.* **102**(17), 175501 (2009)
- Dahmen, K.A.: Mean field theory of slip statistics. In: Salje, E., Planes, A. (eds.) *Avalanches in Functional Materials and Geophysics*, pp. 19–30. Springer, Berlin (2017)
- Sun, Q., Jin, F., Liu, J., Zhang, G.: Understanding force chains in dense granular materials. *Intl. J. Modern Phys. B* **24**(29), 5743–5759 (2010)
- Salerno, K.M., Maloney, C.E., Robbins, M.O.: Avalanches in strained amorphous solids: does inertia destroy critical behavior? *Phys. Rev. Lett.* **109**(10), 105703 (2012)
- Lin, J., Wu, W., Borja, R.I.: Micropolar hypoplasticity for persistent shear band in heterogeneous granular materials. *Comput. Methods Appl. Mech. Eng.* **289**, 24–43 (2015)
- Michlmayr, G., Or, D.: Mechanisms for acoustic emissions generation during granular shearing. *Granul. Matter* **16**(5), 627–640 (2014)
- Li, J., Spaepen, F., Hufnagel, T.C.: Nanometre-scale defects in shear bands in a metallic glass. *Philos. Mag. A* **82**(13), 2623–2630 (2002)

38. Tordesillas, A.: Force chain buckling, unjamming transitions and shear banding in dense granular assemblies. *Philos. Mag.* **87**(32), 4987–5016 (2007)
39. Tordesillas, A., Muthuswamy, M.: On the modeling of confined buckling of force chains. *J. Mech. Phys. Solids* **57**(4), 706–727 (2009)
40. Tordesillas, A., Steer, C.A.H., Walker, D.M.: Force chain and contact cycle evolution in a dense granular material under shallow penetration. *Nonlinear Process. Geophys.* **21**(2), 505–519 (2014)
41. Kuhn, M.R.: Contact transience during slow loading of dense granular materials. *J. Eng. Mech.* **143**(1), 1–9 (2016). [https://doi.org/10.1061/\(ASCE\)EM.1943-7889.0000992](https://doi.org/10.1061/(ASCE)EM.1943-7889.0000992)
42. Sethna, J.P., Dahmen, K.A., Myers, C.R.: Crackling noise. *Nature* **410**(6825), 242 (2001)
43. Tordesillas, A., Zhang, J., Behringer, R.: Buckling force chains in dense granular assemblies: physical and numerical experiments. *Geomech. Geoeng Int. J.* **4**(1), 3–16 (2009)
44. Kuhn, M.R., Bagi, K.: Contact rolling and deformation in granular media. *Int. J. Solids Struct.* **41**(21), 5793–5820 (2004)
45. Radjai, F., Wolf, D.E., Jean, M., Moreau, J.-J.: Bimodal character of stress transmission in granular packings. *Phys. Rev. Lett.* **80**(1), 61–64 (1998)
46. Karmakar, S., Lerner, E., Procaccia, I.: Statistical physics of the yielding transition in amorphous solids. *Phys. Rev. E* **82**(5), 055103 (2010)
47. Hentschel, H.G.E., Jaiswal, P.K., Procaccia, I., Sastry, S.: Stochastic approach to plasticity and yield in amorphous solids. *Phys. Rev. E* **92**(6), 062302 (2015)
48. Calvetti, F., Viggiani, G., Tamagnini, C.: A numerical investigation of the incremental behavior of granular soils. *Rivista Italiana di Geotecnica* **3**, 11–29 (2003)
49. Plassiard, J.-P., Belheine, N., Donzé, F.-V.: A spherical discrete element model: calibration procedure and incremental response. *Granul. Matter* **11**(5), 293–306 (2009)
50. Kuhn, M.R., Mitchell, J.K.: Modelling of soil creep with the discrete element method. *Eng. Comput.* **9**(2), 277–287 (1992)
51. Jäger, J.: Uniaxial deformation of a random packing of particles. *Arch. Appl. Mech.* **69**(3), 181–203 (1999)
52. Walton, K.: The oblique compression of two elastic spheres. *J. Mech. Phys. Solids* **26**(3), 139–150 (1978)
53. da Cruz, F., Emam, S., Prochnow, M., Roux, J.-N., Chevoir, F.: Rheophysics of dense granular materials: discrete simulation of plane shear flows. *Phys. Rev. E* **72**(2), 021309 (2005)
54. Ng, T.-T.: Input parameters of discrete element methods. *J. Eng. Mech.* **132**(7), 723–729 (2006)
55. Suzuki, K., Kuhn, M.R.: Uniqueness of discrete element simulations in monotonic biaxial shear tests. *Int. J. Geomech.* **14**(5), 06014010 (2014). [https://doi.org/10.1061/\(ASCE\)GM.1943-5622.0000365](https://doi.org/10.1061/(ASCE)GM.1943-5622.0000365)